

RIS-Assisted MIMO CV-QKD at THz Frequencies: Channel Estimation and SKR Analysis

Sushil Kumar, Soumya P. Dash, *Senior Member, IEEE*, Debasish Ghose, *Senior Member, IEEE*,
and George C. Alexandropoulos, *Senior Member, IEEE*

Abstract—In this paper, a multiple-input multiple-output (MIMO) wireless system incorporating a reconfigurable intelligent surface (RIS) to efficiently operate at terahertz (THz) frequencies is considered. The transmitter, Alice, employs continuous-variable quantum key distribution (CV-QKD) to communicate secret keys to the receiver, Bob, which utilizes either homodyne or heterodyne detection. The latter node applies the least-squared approach to estimate the effective MIMO channel gain matrix prior to receiving the secret key, and this estimation is made available to Alice via an error-free feedback channel. An eavesdropper, Eve, is assumed to employ a collective Gaussian entanglement attack on the feedback channel to avail the estimated channel state information. We present a novel closed-form expression for the secret key rate (SKR) performance of the proposed RIS-assisted THz CV-QKD system. The effect of various system parameters, such as the number of RIS elements and their phase configurations, the channel estimation error, and the detector noise, on the SKR performance are studied via numerical evaluation of the derived formula. It is demonstrated that the RIS contributes to larger SKR for larger link distances, and that heterodyne detection is preferable over homodyne at lower pilot symbol powers.

Index Terms—Continuous variable quantum key distribution, reconfigurable intelligent surfaces, MIMO, channel estimation, secret key rate.

I. INTRODUCTION

The upcoming sixth-generation (6G) of wireless networks is expected to attain extraordinary capabilities, featuring peak data rates in the order of Tbps, ultra-low latency, and a twofold increase in both spectrum and energy efficiencies relative to its preceding fifth-generation (5G) [1], [2]. To satisfy these stringent requirements, various supporting technologies are being investigated, including ultra massive multiple-input multiple-output (MIMO) systems [3], [4], [5], reconfigurable intelligent surfaces (RISs) [6], [7], [8], [9], [10], and the utilization of terahertz (THz) frequency ranges [11], [12].

As network capacity and connectivity increase, security issues escalate, requiring innovative strategies for secure communication links. Quantum key distribution (QKD) is emerging as a viable approach for ensuring robust, quantum-resistant security and vulnerability to eavesdropping. The

significant advancements in quantum computing make traditional higher-layer encryption schemes based on the Rivest-Shamir-Adleman (RSA) algorithm susceptible to Shor's factoring algorithm [13], [14]. Similarly, the security of physical-layer encryption, which uses conventional key distribution algorithms like Diffie-Hellman, is insecure because it relies on the assumption that classical computers cannot solve the computationally intensive problem of distinct logarithms in a reasonable amount of time [15]. Consequently, contemporary computationally secure encryption techniques may be compromised due to the significant advancements in practical quantum computing. QKD enables safe transmissions of secret keys between two entities, such as Alice and Bob, which can be utilized for one-time-pad cryptography for 6G the physical-layer applications [16]. QKD uses quantum mechanics to safely send cryptographic keys, providing proven protection from the threats that come with quantum computing [17], [18], [19]. There are two principal categories of QKD protocols [17], [20]: discrete variable QKD (DV-QKD), which utilizes single-photon sources along with polarization or time-bin encoding, and continuous variable QKD (CV-QKD), which employs conventional coherent optical sources and homodyne or heterodyne detectors, facilitating integration with existing telecommunications infrastructure [13], [21]. DV-QKD offers strong security, but its reliance on complicated single-photon technology makes it difficult to use on a large scale [22], [23]. On the other hand, CV-QKD is easier to integrate with the existing hardware for wireless communications, opening the door to scalable, quantum-secure 6G networks [24], [25].

On another front, RISs have recently emerged as a promising technology for controlling the propagation of electromagnetic waves in wireless systems [26], [27], [28]. By adjusting the phase of incoming signals, an RIS can manipulate the properties of reflected waves, thereby improving signal coverage, strength, and reliability [29], [30], [31], and thus, it is aimed to operate across a broad range of frequencies, including microwave and millimeter-wave (mmWave) [32], as well as THz bands [33], [34], [35]. Specifically, RISs have been shown to alleviate the challenges in wireless channels faced due to obstructions, signal degradation, or restricted line-of-sight (LoS) pathways [36], especially at elevated frequencies like mmWave and THz [37], resulting in communication systems with ultra-high speeds, minimal latency, and extensive connectivity [38], [39], [40], [41], [42], [43], [44].

Over the past few years, researchers have attempted to combine the latter emerging technologies to examine the feasibility of THz CV-QKD systems. The authors in [45] studied quantum communications with QKD within a micro-

S. Kumar and S. P. Dash are with the School of Electrical Sciences, Indian Institute of Technology Bhubaneswar, Argul, Khordha, 752050 India e-mail: (a24ec09010@iitbbs.ac.in, soumyapdash@iitbbs@gmail.com).

D. Ghose is with the School of Economics, Innovation, and Technology at Kristiania University College, Bergen (e-mail: Debasish.Ghose@kristiania.no).

G. C. Alexandropoulos is with the Department of Informatics and Telecommunications, National and Kapodistrian University of Athens, Panepistimiopolis Iliissia, 15784 Athens, Greece and also with the Department of Electrical and Computer Engineering, University of Illinois Chicago, IL 60601, USA (e-mail: alexandrg@di.uoa.gr).

satellite framework in low-earth-orbit scenarios. A physical hardware architecture of a QKD system operating at the THz was designed in [46]. The viability of elevated key rates and extended distances in THz CV-QKD by applying multi-carrier multiplexing in inter-satellite communication links was demonstrated in [47]. However, in all these studies, the presented THz QKD systems attained low secret key rates (SKRs) and short maximum transmission distances due to the high atmospheric absorption loss and free-space path loss. To overcome this, the use of MIMO was found to be a viable option. The authors in [48] considered a MIMO THz QKD scheme capable to obtain positive SKRs in the 10 – 30 THz frequency spectrum. The impact of the channel estimation error on SKR for MIMO CV-QKD wireless communication system at THz was studied in [16].

Very recently, the technology of RISs was considered in QKD system designs. The authors in [49] analyzed the SKR performance under log-normal fading turbulence conditions for an RIS-assisted free-space optical system. An RIS-assisted MIMO THz CV-QKD system that attains a high SKR and extensive transmission lengths compared to a non-RIS counterpart was presented in [50]. However, both studies assumed the possession of flawless channel information by both Alice and Bob, which is impractical. In fact, to the best of the authors' knowledge, there does not exist any investigation in the open technical literature of the impact of channel estimate errors on the SKR of RIS-assisted MIMO CV-QKD systems.

Motivated by the latter research gap, in this paper, we consider an RIS-assisted MIMO THz system where the transmitter, Alice, wishes to send secret keys to the receiver, Bob, using CV-QKD. A pragmatic channel estimation approach, based on the least-squares (LS) technique, is employed at Bob to estimate the effective MIMO channel prior to secret key reception. The estimated channel state information is then provided to Alice via an error-free feedback channel, which is attacked by an eavesdropper, Eve, using a collective Gaussian entanglement attack. We analyze the SKR performance of the system considering the impact of channel estimate errors into the transmit-receive model during the key generation phase. The contributions of the paper are summarized as follows:

- We present an LS-based channel estimation protocol according to which Alice and Bob design their beamforming matrices via the singular-value decomposition (SVD) of the estimated effective MIMO channel matrix.
- The input-output relationship between Alice and Bob throughout the key generation phase is established, which includes the supplementary noise factors resulting from channel estimate inaccuracies as well as the detector noise arising due to Bob employing either homodyne or heterodyne detection for the secret key reception.
- The variance of the latter supplementary noise components is delineated to obtain a novel closed-form expression for the SKR performance of the considered RIS-assisted MIMO CV-QKD system. The derived expression considers both types of measurements at Bob's side, integrating the impacts of channel estimation overhead as well as the supplementary noise components resulting from imperfect channel estimation.

- Comprehensive numerical simulations are conducted to investigate the impact of the channel estimate error and evaluate the influence of critical parameters, such as pilot length and pilot power, on the system's SKR performance. The roles of the number and phase configuration of the RIS elements on the SKR metric are examined, as well as those of the choice of the measurement approach at Bob and the physical distance between Alice and Bob.

The rest of the paper is organized as follows. The RIS-assisted MIMO CV-QKD system model and the THz channel model are presented in Section II. The proposed channel estimation protocol is introduced in Section III. Section IV details the secret key generation, transmission, and measurement phases based on the evaluation of the covariance matrix of the noise arising due to imperfect channel information. The SKR analysis for both homodyne and heterodyne measurements considering that Eve deploys a collective Gaussian entanglement attack is presented in Section V. The numerical results of the paper are presented in Section VI, followed by its concluding remarks in Section VII.

Notation: Bold (\mathbf{A}) and (\mathbf{a}) letters stand for matrices and vectors, respectively. \mathbf{A}^\dagger symbol stands for the conjugate transpose of \mathbf{A} , while \mathbf{A}^T its transpose. Notations $\mathbf{1}_{M \times N}$ and $\mathbf{0}_{M \times N}$ represent a $M \times N$ matrix consisting of all ones and all zeros, respectively, and $j \triangleq \sqrt{-1}$. \mathbf{I}_M represents the $M \times M$ identity matrix, and $\text{diag}(\mathbf{a})$ with $\mathbf{a} \in \mathbb{C}^M$ returns a $M \times M$ diagonal matrix with the elements of \mathbf{a} on its principal diagonal. a^* represents the conjugate of a . Notation $\mathcal{N}(\boldsymbol{\mu}, \boldsymbol{\Sigma})$ represents the real multivariate Gaussian distribution, where $\boldsymbol{\mu}$ is the mean vector and $\boldsymbol{\Sigma}$ is the covariance matrix, $|\cdot|$ denotes the magnitude operator. Finally, $\mathbf{E}[\cdot]$ is the expectation operator and $\text{Tr}(\cdot)$ is the trace operator.

II. SYSTEM MODEL

We consider an RIS-assisted MIMO CV-QKD setup as depicted in Fig. 1a. The transmitter, referred to as Alice, and the receiver, referred to as Bob, are equipped with N_T and N_R antennas, respectively, and there exists a direct LoS channel between them together with a virtual LoS channel via an RIS. The RIS comprises K passive reflecting elements that can be optimized to adjust the phases of the incoming information-bearing signals [28]. Thus, the overall MIMO channel between Alice and Bob considering the RIS-assisted path as well as the direct Alice-Bob path, which is denoted by $\mathbf{H}_{\text{RIS}} \in \mathbb{C}^{N_R \times N_T}$, can be expressed as follows:

$$\mathbf{H}_{\text{RIS}} \triangleq \mathbf{H}_d + \mathbf{H}_f \boldsymbol{\Phi}_{\text{RIS}} \mathbf{H}_g, \quad (1)$$

where $\boldsymbol{\Phi}_{\text{RIS}} \triangleq \text{diag}(e^{j\phi_1}, \dots, e^{j\phi_K})$ with ϕ_k denoting the phase shift introduced by each k -th ($k = 1, \dots, K$) reflective element of the RIS. Furthermore, $\mathbf{H}_d \in \mathbb{C}^{N_R \times N_T}$, $\mathbf{H}_g \in \mathbb{C}^{K \times N_T}$, and $\mathbf{H}_f \in \mathbb{C}^{N_R \times K}$ are the channel gain matrices between Alice and Bob, Alice and RIS, and RIS and Bob, respectively, which are modeled for the considered in this paper THz frequency spectrum as follows:

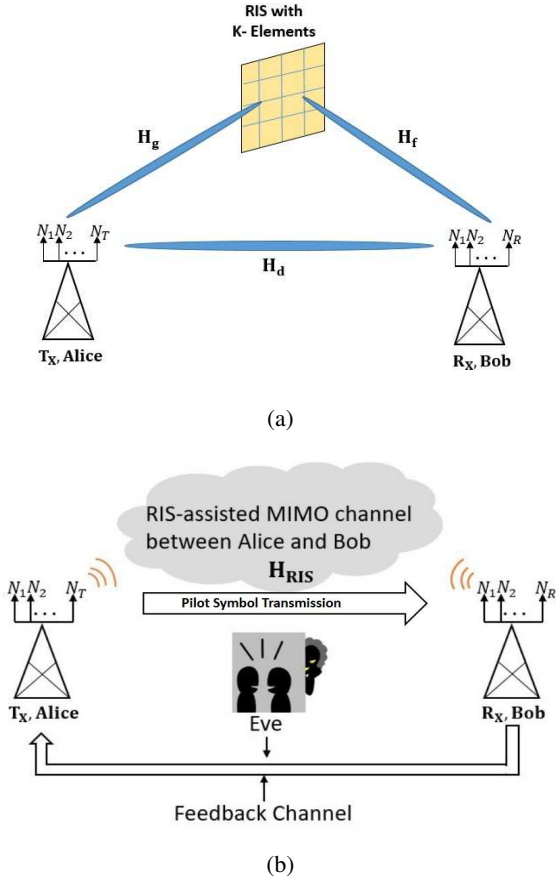


Fig. 1: (a) The considered RIS-assisted MIMO CV-QKD wireless communication system at THz frequencies; (b) The feedback channel designed to transfer the estimated MIMO channel at Bob's side to Alice, which is eavesdropped by Eve.

$$\begin{aligned}
 \mathbf{H}_d &\triangleq \sum_{l=1}^L \sqrt{\delta_{d,l}} e^{j2\pi f_c \tau_{d,l}} \mathbf{h}_{N_R}(\theta_l^{R_x}) \mathbf{h}_{N_T}^\dagger(\theta_l^{T_x}), \\
 \mathbf{H}_g &\triangleq \sum_{m=1}^M \sqrt{\delta_{g,m}} e^{j2\pi f_c \tau_{g,m}} \mathbf{h}_{\text{RIS}}(\varphi, \theta_m^{\text{RIS}}) \mathbf{h}_{N_T}^\dagger(\theta_m^{T_x}), \\
 \mathbf{H}_f &\triangleq \sum_{n=1}^N \sqrt{\delta_{f,n}} e^{j2\pi f_c \tau_{f,n}} \mathbf{h}_{N_R}(\theta_n^{R_x}) \mathbf{h}_{\text{RIS}}^\dagger(\varphi, \theta_n^{\text{RIS}}), \quad (2)
 \end{aligned}$$

where L , M , and N denote the number of signal propagation paths within the wireless channels \mathbf{H}_d , \mathbf{H}_g , and \mathbf{H}_f , respectively. In addition, f_c is the carrier frequency, and $\tau_{d,l}$, $\tau_{g,m}$, $\tau_{f,n}$ and $\delta_{d,l}$, $\delta_{g,m}$, $\delta_{f,n}$ are the propagation delays and path losses corresponding to the l -th path of \mathbf{H}_d , m -th path of \mathbf{H}_g , and n -th path of \mathbf{H}_f , respectively. Moreover, $\theta_l^{T_x}$, $\theta_m^{T_x}$, and θ_n^{RIS} represent the respective angles of departure (AoDs), and $\theta_l^{R_x}$, θ_m^{RIS} , and $\theta_n^{R_x}$ are the respective angles of arrival (AoAs) from the transmitter's and to the receiver's uniform linear arrays (ULAs), respectively. The antenna elements in both ULAs are considered to be uniformly placed in a single dimension such that the inter-element spacing is maintained at d_a . This results in the following expression for both the array response vectors \mathbf{h}_{N_T} and \mathbf{h}_{N_R} :

$$\mathbf{h}_N(\theta) \triangleq \frac{1}{\sqrt{N}} \left[1, e^{j\frac{2\pi}{\lambda_c} d_a \sin \theta}, \dots, e^{j\frac{2\pi}{\lambda_c} d_a (N-1) \sin \theta} \right]^T, \quad (3)$$

where $N \in \{N_T, N_R\}$ and $\lambda_c = c/f_c$ with c being the speed of light. Finally, the vector $\mathbf{h}_{\text{RIS}} \in \mathbb{C}^{K \times 1}$ in (2) indicates the ULA of the RIS and is given as follows [51], [52]:

$$\mathbf{h}_{\text{RIS}}(\varphi, \theta_i^{\text{RIS}}) \triangleq \frac{1}{\sqrt{K}} \begin{bmatrix} e^{j\frac{2\pi}{\lambda_c} (\vartheta_X^{\varphi, \theta_i^{\text{RIS}}} + \vartheta_Y^{\varphi, \theta_i^{\text{RIS}}})}, \dots \\ \dots, e^{j\frac{2\pi}{\lambda_c} ((K_X-1)\vartheta_X^{\varphi, \theta_i^{\text{RIS}}} + (K_Y-1)\vartheta_Y^{\varphi, \theta_i^{\text{RIS}}})} \end{bmatrix}^T, \quad (4)$$

where we have used the definitions for $i = m$ and $i = n$:

$$\begin{aligned}
 \vartheta_X^{\varphi, \theta_i^{\text{RIS}}} &\triangleq d_X \cos(\varphi) \sin(\theta_i^{\text{RIS}}), \\
 \vartheta_Y^{\varphi, \theta_i^{\text{RIS}}} &\triangleq d_Y \sin(\varphi) \sin(\theta_i^{\text{RIS}}). \quad (5)
 \end{aligned}$$

The RIS elements are considered to be arranged along a two-dimensional structure [53], [54] with K_X and K_Y reflecting elements being placed along the horizontal and vertical axes, respectively, implying that $K_X K_Y = K$. Further, the separation between the elements in the corresponding axes is denoted by d_X and d_Y , and the path losses in (2) are expressed as:

$$\delta_{j,i} \triangleq \begin{cases} \left(\frac{\lambda_c}{4\pi d_{j,i}} \right)^2 G_T G_R 10^{-0.1\rho d_{j,i}}, & j \in \{d, g, f\}, i = 1 \\ \zeta \xi_i \left(\frac{\lambda_c}{4\pi d_{j,i}} \right)^2 G_T G_R 10^{-0.1\rho d_{j,i}}, & i \in \{l, m, n \neq 1\} \end{cases}, \quad (6)$$

where $d_{j,i}$ is the smallest path length, ξ_i is the Fresnel reflection coefficient of each i -th multipath component, ζ is the Rayleigh roughness factor, and ρ (in dB/km) is the atmospheric absorption loss. Moreover, the ULA gains at Alice and Bob are $G_T \triangleq N_T G_a$ and $G_R \triangleq N_R G_a$, respectively, where G_a represents the gain of each component of the transmitter and receiver antennas and G_T (or G_R) = K when the data symbols are transmitter from (or to) the RIS, respectively.

III. PROPOSED LS CHANNEL ESTIMATION PROTOCOL

In this paper, we focus on the practical setting for our RIS-assisted MIMO CV-QKD system where Bob performs estimation of the effective MIMO channel \mathbf{H}_{RIS} in (1) before the actual key distribution protocol between this receiver and Alice becomes operational. As previously discussed and depicted in Fig. 1a, our system supports a seamless feedback link between Bob and Alice, where the former communicates to the latter its estimated channel parameters that will be used in the next phase by Alice for the key distribution and the actual data transmission. We assume that the eavesdropper Eve attempts to intercept the feedback link to obtain Bob's estimation, i.e., the estimation of the RIS-assisted MIMO between Alice and Bob, as shown in Fig. 1b.

To enable channel estimation, Alice transmits L_p pilot signals to Bob via the effective MIMO channel \mathbf{H}_{RIS} [55]. It is assumed that this channel is quasi-static, implying that \mathbf{H}_{RIS} remains constant throughout the channel coherence time T_c , thus, it must hold $L_p < T_c$. The pilot symbols are constructed by using the position and momentum quadratures to create Gaussian coherent states [48], [56], hence, the $N_T \times 1$ pilot symbol vector during each ℓ -th transmission duration ($\ell = 1, \dots, L_p$) is represented by $\psi_p^\ell \triangleq \mathbf{x}_p^\ell + j\mathbf{p}_p^\ell$, where $\mathbf{x}_p^\ell \triangleq [x_{p,1}^\ell, \dots, x_{p,N_T}^\ell]^T$, $\mathbf{p}_p^\ell \triangleq [p_{p,1}^\ell, \dots, p_{p,N_T}^\ell]^T$, and $\psi_p^\ell \sim$

$\mathcal{CN}(\mathbf{0}_{N_T}, 2V_p \mathbf{I}_{N_T})$. Upon reception of the pilot symbols, Bob performs heterodyne measurements, implying that both the position and momentum quadratures of the received signal mode are measured. To this end, the complex-valued N_R -element received vector at each ℓ -th pilot duration can be mathematically expressed as follows:

$$\mathbf{y}_p^\ell \triangleq \mathbf{H}_{\text{RIS}} \psi_p^\ell + \mathbf{H}_{\text{RIS}} \psi_0^\ell + \mathbf{n}_{\text{het}}^\ell, \quad (7)$$

where $\mathbf{n}_{\text{het}}^\ell \triangleq \mathbf{n}_{\text{het},I}^\ell + j\mathbf{n}_{\text{het},Q}^\ell$ is the additive noise vector at the receiver arising due to the heterodyne measurement, with $\mathbf{n}_{\text{het},I}^\ell, \mathbf{n}_{\text{het},Q}^\ell \sim \mathcal{N}(\mathbf{0}_{N_R \times 1}, (2\nu_{en} + 1)\mathbf{I}_{N_R})$ being respectively the in-phase and quadrature-phase components, respectively, where ν_{en} being is variance of the electronic noise. Note that, $\psi_0^\ell = \mathbf{x}_0^\ell + j\mathbf{p}_0^\ell$ is the preparation thermal noise at the side of Alice with $\mathbf{x}_0^\ell, \mathbf{p}_0^\ell \sim \mathcal{N}(\mathbf{0}_{N_T \times 1}, V_0 \mathbf{I}_{N_T})$. Here $V_0 \triangleq 2\bar{n} + 1$ is the thermal noise variance with $\bar{n} \triangleq [\exp(hf_c/k_B T_e) - 1]^{-1}$, where h is the Plank's constant, k_B is the Boltzmann's constant, and T_e is the environmental temperature in Kelvin. By collecting all L_p pilot symbols, the following vector-matrix expression is deduced from (7):

$$\mathbf{Y}_p = \mathbf{H}_{\text{RIS}} \Psi_p + \mathbf{H}_{\text{RIS}} \Psi_0 + \mathbf{N}_{\text{het}}, \quad (8)$$

where $\mathbf{Y}_p \triangleq [\mathbf{y}_p^1, \dots, \mathbf{y}_p^{L_p}] \in \mathbb{C}^{N_R \times L_p}$, $\Psi_p \triangleq [\mathbf{x}_p^1, \dots, \mathbf{x}_p^{L_p}] \in \mathbb{C}^{N_T \times L_p}$, and $\mathbf{N}_{\text{het}} \triangleq [\mathbf{n}_{\text{het}}^1, \dots, \mathbf{n}_{\text{het}}^{L_p}] \in \mathbb{C}^{N_R \times L_p}$. By defining $\tilde{\mathbf{N}} \triangleq \mathbf{H}_{\text{RIS}} \Psi_0 + \mathbf{N}_{\text{het}}$ as the equivalent noise matrix, (8) can be re-written as follows:

$$\mathbf{Y}_p = \mathbf{H}_{\text{RIS}} \Psi_p + \tilde{\mathbf{N}}. \quad (9)$$

As expected, to enable explicit channel estimation, the pilot matrix Ψ_p is known at both Alice and Bob. However, the covariance matrix of $\tilde{\mathbf{N}}$ included in (8), including the unknown \mathbf{H}_{RIS} , is unknown. To this end, by applying the LS approach, \mathbf{H}_{RIS} can be estimated from (8) at Bob as follows:

$$\begin{aligned} \mathbf{H}_{\text{RIS,LS}} &\stackrel{(a)}{=} \mathbf{Y}_p \Psi_p^\dagger (\Psi_p \Psi_p^\dagger)^{-1} \\ &\stackrel{(b)}{=} \mathbf{H}_{\text{RIS}} + \underbrace{\tilde{\mathbf{N}} \Psi_p^\dagger (\Psi_p \Psi_p^\dagger)^{-1}}_{\triangleq \Delta \mathbf{H}_{\text{RIS}}}, \end{aligned} \quad (10)$$

where step (b) is obtained by substituting (9) in (a). Note that LS-optimal channel estimation performance is obtained when Ψ_p is constructed such that its rows are orthogonal and the norm of each row is equal to $\sqrt{V_p L_p}$. These conditions are met when using the discrete Fourier transform (DFT) matrix [16]. In this case, Ψ_p is given by:

$$\begin{aligned} \Psi_p &= \sqrt{V_p} \\ &\times \begin{bmatrix} 1 & 1 & \dots & 1 \\ 1 & e^{j2\pi/L_p} & \dots & e^{j2\pi(L_p-1)/L_p} \\ \vdots & \vdots & \dots & \vdots \\ 1 & e^{j2\pi(N_T-1)/L_p} & \dots & e^{j2\pi(N_T-1)(L_p-1)/L_p} \end{bmatrix}. \end{aligned} \quad (11)$$

When the estimated channel matrix is obtained, Bob occupies the feedback channel, which is assumed to be a classical public authenticated channel, to transfer the estimated coefficients of the RIS-assisted MIMO channel to Alice.

IV. SECRET KEY GENERATION AND PROCESSING

After acquiring the estimated channel, Alice employs CV-QKD based on Gaussian modulation to encrypt the secret keys intended for Bob via the RIS-assisted wireless channel. To attain this, the two N_T -element random vectors \mathbf{x}_A and \mathbf{p}_A are generated, which correspond to the position and momentum quadratures of the secret key states. These vectors are statistically independent and adhere to zero-mean Gaussian distributions, i.e., $\mathbf{x}_A, \mathbf{p}_A \sim \mathcal{N}(\mathbf{0}_{N_T \times 1}, V_s \mathbf{I}_{N_T})$ with V_s denoting the variance utilized for encoding the secret key information. Hence, the secret key is transmitted as the vector $\psi = \mathbf{x}_A + j\mathbf{p}_A$ from Alice's antenna elements.

Recall that the estimation of the effective channel $\mathbf{H}_{\text{RIS,LS}}$, available to Alice and Bob, has been also made available to Eve via eavesdropping. Let r and β_1, \dots, β_r denote respectively this channel's rank and r non-zero singular values. Applying SVD yields $\mathbf{H}_{\text{RIS,LS}} = \mathbf{U}_{\text{RIS,LS}} \Sigma_{\text{RIS,LS}} \mathbf{V}_{\text{RIS,LS}}^\dagger$, where

$$\Sigma_{\text{RIS,LS}} \triangleq \begin{bmatrix} \text{diag}(\sqrt{\beta_1}, \dots, \sqrt{\beta_r}) & \mathbf{0}_{r \times (N_T-r)} \\ \mathbf{0}_{(N_R-r) \times r} & \mathbf{0}_{(N_R-r) \times (N_T-r)} \end{bmatrix} \quad (12)$$

with $\mathbf{V}_{\text{RIS,LS}} \in \mathbb{C}^{N_T \times N_T}$ and $\mathbf{U}_{\text{RIS,LS}} \in \mathbb{C}^{N_R \times N_R}$ being unitary matrices. This implies that Alice and Bob can respectively utilize $\mathbf{V}_{\text{RIS,LS}}$ and $\mathbf{U}_{\text{RIS,LS}}$ for transmit beamforming and receive combining, respectively. In addition, Eve can apply the latter matrices to $\mathbf{H}_{\text{RIS,LS}}$ to extract $\Sigma_{\text{RIS,LS}}$ that carries the secret keys. To this end, Eve uses a collective entanglement attack [48], [57] by creating a pair of two-mode squeezed vacuum (TMSV) modes $\{e_{in_i}, e_{qm_i}\} \forall i = 1, \dots, N_T$ (also known as EPR pair), where e_{in_i} is injected into Alice's transmitted signal and e_{qm_i} is stored in the eavesdropper's quantum memory. Thus, the post-processed N_R -element received signal mode vector at Bob's side can be expressed as follows:

$$\mathbf{b} \triangleq \mathbf{U}_{\text{RIS,LS}}^\dagger (\mathbf{H}_{\text{RIS}} \mathbf{V}_{\text{RIS,LS}} \psi + \mathbf{U}_{\text{RIS,LS}} \mathbf{S}_{\text{RIS,LS}} \mathbf{e}), \quad (13)$$

where $\psi \triangleq [\psi_1, \dots, \psi_{N_T}]^T$ denotes Alice's transmitting mode, $\mathbf{b} \triangleq [b_1, \dots, b_{N_R}]^T$ is the received mode at Bob, and $\mathbf{e} \triangleq [e_1, \dots, e_{N_T}]^T$ includes the Gaussian noise contributions injected by Eve to extract the secret key. In addition, the diagonal matrix $\mathbf{S}_{\text{RIS,LS}}$ in (13) is given as:

$$\mathbf{S}_{\text{RIS,LS}} \triangleq \begin{bmatrix} \text{diag}(\sqrt{1-\beta_1}, \dots, \sqrt{1-\beta_r}) & \mathbf{0}_{r \times (N_T-r)} \\ \mathbf{0}_{(N_R-r) \times r} & \mathbf{J}_{(N_R-r) \times (N_T-r)} \end{bmatrix}, \quad (14)$$

where matrix \mathbf{J} is defined as follows:

$$\mathbf{J} \triangleq \begin{bmatrix} \mathbf{I}_{N_1} & \mathbf{0}_{N \times (N_T-N_R)} \\ \mathbf{0}_{(N_R-N_T) \times N} & \mathbf{I}_{N_2} \end{bmatrix}, \quad (15)$$

where $N = \min((N_R - r), (N_T - r))$ and $N_1 + N_2 = N$.

By substituting expression (10) for the estimated channel in (13) and defining the channel estimation error matrix $\Delta \mathbf{H}_{\text{RIS}} \triangleq \mathbf{H}_{\text{RIS,LS}} - \mathbf{H}_{\text{RIS}}$, vector \mathbf{b} can be re-expressed as:

$$\mathbf{b} = \Sigma_{\text{RIS,LS}} \psi - \underbrace{\mathbf{U}_{\text{RIS,LS}}^\dagger \Delta \mathbf{H}_{\text{RIS}} \mathbf{V}_{\text{RIS,LS}} \psi}_{\triangleq \mathbf{n}_{\text{RIS}}} + \mathbf{S}_{\text{RIS,LS}} \mathbf{e}, \quad (16)$$

where $\mathbf{n}_{\text{RIS}} \in \mathbb{C}^{N_R \times 1}$ indicates the additional noise term that occurs as a result of the channel estimation errors.

Upon receiving \mathbf{b} , Bob conducts measurements to extract the confidential key information. It is to be recollected that

during the channel estimation process, Bob utilized heterodyne measurements to estimate the effective channel \mathbf{H}_{RIS} , which entailed quantifying both the position and momentum quadratures of the incoming signal. However, during the key reception phase, we consider that Bob may perform either homodyne or heterodyne measurements. To this end, the measurement output of one or both real-valued quadratures can yield the secret key. Following the measurement, the correlation between Alice's input and Bob's output, delineated in terms of the quadratures, is computed $\forall i = 1, 2, \dots, r$ as:

$$\hat{Q}_{b_i} \triangleq \sqrt{\beta_i} \hat{Q}_{a_i} + \sqrt{1 - \beta_i} \hat{Q}_{e_i} - n_{\text{RIS}_i} + n_{d_i}, \quad (17)$$

and subsequently, Eve's output mode can be expressed in terms of the quadratures $\forall i = 1, 2, \dots, r$ as follows:

$$\hat{Q}_{e_{o_i}} \triangleq -\sqrt{1 - \beta_i} \hat{Q}_{a_i} + \sqrt{\beta_i} \hat{Q}_{e_i} - n_{\text{RIS}_i}, \quad (18)$$

where \hat{Q}_{b_i} represents the measurement output of Bob's quadrature, \hat{Q}_{a_i} denotes Alice's transmitted quadrature, and \hat{Q}_{e_i} represents the quadrature of the mode injected by Eve to extract crucial information, all each i -th coherent state. In addition, all \hat{Q} 's in (17) and (18) denote one of the two quadratures, namely, either the position or momentum quadrature. Due to the presence of the preparation thermal noise, the variance of the quadrature corresponding to Alice's transmitted mode is given as $\text{var}(\hat{Q}_{a_i}) \triangleq V_a = V_s + V_o$. Similarly, the variance of the measurement occurring due to Eve's injected TMSV modes is defined $\text{var}(\hat{Q}_{e_i}) \triangleq V_e$. Owing to the statistics of the channel estimation noise, n_{RIS_i} follows a zero-mean Gaussian distribution, implying that $n_{\text{RIS}_i} \sim \mathcal{N}(0, \sigma_{\text{RIS}_i}^2)$ with $\sigma_{\text{RIS}_i}^2 = 0.5 \mathbf{C}_{\text{RIS}}(i, i)$ where \mathbf{C}_{RIS} represents the covariance matrix of the extra noise vector \mathbf{n}_{RIS} in (17). Additionally, n_{d_i} denotes the detection noise arising during Bob's measurement, which also follows a zero-mean Gaussian distribution with a variance $\sigma_{d_i}^2 \triangleq d_m(\nu_{en} + 1) - 1$, i.e., $n_{d_i} \sim \mathcal{N}(0, \sigma_{d_i}^2)$, where d_m takes the values 1 or 2 for homodyne or heterodyne measurements, respectively.

The SKR of the system can be computed based on the available measurements in (17). Hence, the secret key can be employed for key encryption and subsequent transmission, conditioned on the computed SKR being above a pre-decided threshold. However, for the SKR computation, the value of $\sigma_{\text{RIS}_i}^2$ must be ascertained to Alice and Bob, implying that the covariance matrix of \mathbf{n}_{RIS} needs to be estimated. Using (16) this covariance matrix, defined as $\mathbf{C}_{\text{RIS}} \in \mathbb{C}^{N_R \times N_R}$, can be expressed as follows:

$$\begin{aligned} \mathbf{C}_{\text{RIS}} &\triangleq \mathbf{E} \left[\mathbf{n}_{\text{RIS}} \mathbf{n}_{\text{RIS}}^\dagger \right] \\ &= \mathbf{E} \left[\mathbf{U}_{\text{RIS}_{\text{LS}}}^\dagger \tilde{\mathbf{N}} \Psi_p^\dagger (\Psi_p \Psi_p^\dagger)^{-1} \mathbf{V}_{\text{RIS}_{\text{LS}}} \psi \psi^\dagger \right. \\ &\quad \left. \times \mathbf{V}_{\text{RIS}_{\text{LS}}}^\dagger (\Psi_p^\dagger \Psi_p)^{-1} \Psi_p \tilde{\mathbf{N}}^\dagger \mathbf{U}_{\text{RIS}_{\text{LS}}} \right] \\ &\stackrel{(a)}{=} 2V_a \mathbf{E} \left[\mathbf{U}_{\text{RIS}_{\text{LS}}}^\dagger \tilde{\mathbf{N}} \Psi_p^\dagger (\Psi_p \Psi_p^\dagger)^{-1} (\Psi_p^\dagger \Psi_p)^{-1} \right. \\ &\quad \left. \times \Psi_p \tilde{\mathbf{N}}^\dagger \mathbf{U}_{\text{RIS}_{\text{LS}}} \right] \\ &\stackrel{(b)}{=} \frac{2V_a}{(V_p L_p)^2} \mathbf{E} \left[\mathbf{U}_{\text{RIS}_{\text{LS}}}^\dagger \tilde{\mathbf{N}} \Psi_p^\dagger \Psi_p \tilde{\mathbf{N}}^\dagger \mathbf{U}_{\text{RIS}_{\text{LS}}} \right] \\ &\stackrel{(c)}{=} \frac{2V_a N_T}{V_p L_p} \mathbf{U}_{\text{RIS}_{\text{LS}}}^\dagger \mathbf{C}_{\tilde{\mathbf{N}}} \mathbf{U}_{\text{RIS}_{\text{LS}}}, \end{aligned} \quad (19)$$

where $\mathbf{E}[\psi \psi^\dagger] = 2V_a \mathbf{I}_{N_T}$ was used in step (a) and $\Psi_p \Psi_p^\dagger = V_p L_p \mathbf{I}_{N_T}$ was used in (b). Furthermore, step (c) follows from [58, Lemma 4] and $\text{Tr}(\Psi_p^\dagger \Psi_p) = V_p N_T L_p$.

Since the noise covariance matrix $\mathbf{C}_{\tilde{\mathbf{N}}} = \mathbf{E}[\tilde{\mathbf{N}} \tilde{\mathbf{N}}^\dagger]$ in (19) is unknown, the first step is to ascertain its maximum likelihood (ML) estimate. This estimate is subsequently utilized to obtain an estimate for \mathbf{C}_{RIS} . The ML estimate of $\mathbf{C}_{\tilde{\mathbf{N}}}$ can be computed using the estimated channel matrix $\mathbf{H}_{\text{RIS}_{\text{LS}}}$ and the known pilot symbol matrix Ψ_p , as follows:

$$\begin{aligned} \hat{\mathbf{C}}_{\tilde{\mathbf{N}}_{\text{ML}}} &\triangleq \arg \max_{\mathbf{C}_{\tilde{\mathbf{N}}}} \log \left(\frac{1}{\pi^{N_R} \det(\mathbf{C}_{\tilde{\mathbf{N}}})} \right. \\ &\quad \left. \times \exp \left\{ -(\mathbf{y}_p^\ell - \mathbf{H}_{\text{RIS}_{\text{LS}}} \psi_p^\ell)^\dagger \mathbf{C}_{\tilde{\mathbf{N}}}^{-1} (\mathbf{y}_p^\ell - \mathbf{H}_{\text{RIS}_{\text{LS}}} \psi_p^\ell) \right\} \right) \\ &= \arg \min_{\mathbf{C}_{\tilde{\mathbf{N}}}} \log (\pi^{N_R} \det(\mathbf{C}_{\tilde{\mathbf{N}}})) \\ &\quad + \sum_{\ell=1}^{L_p} (\mathbf{y}_p^\ell - \mathbf{H}_{\text{RIS}_{\text{LS}}} \psi_p^\ell)^\dagger \mathbf{C}_{\tilde{\mathbf{N}}}^{-1} (\mathbf{y}_p^\ell - \mathbf{H}_{\text{RIS}_{\text{LS}}} \psi_p^\ell). \end{aligned} \quad (20)$$

Solving for $\mathbf{C}_{\tilde{\mathbf{N}}}$ by computing (20)'s derivative, and then, equating it to zero results in the ML estimate of the covariance matrix, which is given by:

$$\hat{\mathbf{C}}_{\tilde{\mathbf{N}}_{\text{ML}}} = \frac{1}{L_p} \sum_{\ell=1}^{L_p} (\mathbf{y}_p^\ell - \mathbf{H}_{\text{RIS}_{\text{LS}}} \psi_p^\ell) (\mathbf{y}_p^\ell - \mathbf{H}_{\text{RIS}_{\text{LS}}} \psi_p^\ell)^\dagger. \quad (21)$$

Therefore, an estimate for \mathbf{C}_{RIS} that can be used to determine the SKR is obtained by substituting (21) in the place of $\mathbf{C}_{\tilde{\mathbf{N}}}$ in (19), yielding:

$$\hat{\mathbf{C}}_{\text{RIS}_{\text{ML}}} = \frac{2V_a N_T}{V_p L_p} \mathbf{U}_{\text{RIS}_{\text{LS}}}^\dagger \hat{\mathbf{C}}_{\tilde{\mathbf{N}}_{\text{ML}}} \mathbf{U}_{\text{RIS}_{\text{LS}}}. \quad (22)$$

V. SKR ANALYSIS

In this section, we analyze the SKR of the considered RIS-assisted MIMO CV-QKD THz system in the presence of channel estimation errors and the overheads derived in Section IV.

Alice and Bob initiate the generation and reception of secret keys with the help of the two strings of correlated random quadrature (as mentioned after (18)) vectors, $\hat{\mathbf{Q}}_{a_m}$ and $\hat{\mathbf{Q}}_{b_m}$, with $m = 1, \dots, (T_c - L_p)$, where, $\hat{\mathbf{Q}}_{a_m}$ represents the transmitted vectors of Gaussian-modulated coherent states by Alice and $\hat{\mathbf{Q}}_{b_m}$ represents vectors of received quadrature states at Bob's end to employ detection technique, through the repetition of the QKD process outlined in Section IV, where T_c represents the channel coherence time and L_p denotes the pilot duration. The repeated execution of the protocol ensures that both gather enough data points to establish a statistically significant correlation needed for secure key generation. To this end, they both perform a reconciliation or sifting protocol over a classical authenticated channel to retrieve the final keys, followed by error correction on the raw keys [59]. Typically, there exist two categories of reconciliation protocols. The first one is known as direct reconciliation (DR), in which Alice specifies the quadrature to be utilized for secret key generation, and the second one is termed reverse reconciliation (RR) according to which Bob indicates the quadrature to be

employed for their measurement for secret key generation via a classical public channel. For the considered RIS-assisted MIMO CV-QKD system, it is expected that RR would result in higher SKR, since Eve who possesses the knowledge of the wireless channel, can extract more information when Alice specifies which quadrature is utilized for the secret key transmission. However, in RR, Bob's measured quadrature remains inaccessible to Eve. Therefore, we concentrate exclusively on RR, as this method can yield positive SKR for any channel transmittance $\beta_i \in [0, 1]$. Conversely, for DR, it is necessary that $\beta_i > 0.5$ to attain positive SKRs [46], [59], which poses practical difficulties due to the considerably elevated path loss at THz frequencies, as given by (6).

Following the secret key transmission, Eve uses a collective entanglement attack to maximize the extraction of key information, in which the received signals from Alice are measured one by one. Upon completion of Bob's measurements, Alice performs a collective measurement on the stored ancilla. To fix the error, Bob employs RR to achieve the positive secret key rate for any channel transmission. For such a setup, the SKR of each i -th ($i = 1, 2, \dots, r$) parallel channel is given as:

$$\text{SKR}_i^{\text{RR}} \triangleq \left(1 - \frac{L_p}{T_c}\right) (\eta I(Q_{a_i}; Q_{b_i}) - I(Q_{b_i}; E_i)), \quad (23)$$

where $I(Q_{a_i}; Q_{b_i})$ represents Shannon's mutual information between Alice's and Bob's measurement results. Similarly, $I(Q_{b_i}; E_i)$ denotes the quantum information (also known as Holevo information) between Eve's and Bob's quantum state for each i -th parallel channel. Furthermore, η denotes the reconciliation efficiency and the term $\left(1 - \frac{L_p}{T_c}\right)$ arises as a result of the channel estimation overhead. In addition, Shannon's mutual information between Alice's and Bob's measurement for each i -th parallel channel is computed as:

$$I(Q_{a_i}; Q_{b_i}) \triangleq \frac{d_m}{2} \log_2 \left(1 + \frac{\beta_i V_s}{\beta_i V_o + (1 - \beta_i) V_e + \sigma_{d_i}^2 + \sigma_{\text{RIS}_i}^2}\right), \quad (24)$$

where $d_m = 1$ or 2 depending on whether Bob performs homodyne or heterodyne measurements, respectively.

A. The Holevo Information

The Holevo information $I(Q_{b_i}; E_i)$, which represents the quantity of information exchanged between Eve and Bob's quantum state for each i -th parallel channel, is expressed as:

$$I(Q_{b_i}; E_i) \triangleq S(E_i) - S(E_i | Q_{b_i}), \quad (25)$$

where $S(E_i)$ and $S(E_i | Q_{b_i})$ denote respectively the Von Neumann entropy of Eve's output state and the conditional Von Neumann entropy of Eve's output state conditioned on Bob's quadrature mode Q_{b_i} . The latter is based on the choice of either homodyne or heterodyne measurements performed by Bob's side. For a given Gaussian quantum state $\tilde{\rho}$ (either E_i or E_i conditioned on Q_{b_i}), the Von Neumann entropy can be expressed as follows [60]:

$$S(\tilde{\rho}) \triangleq \sum_{q=1}^2 h_o(\lambda_q), \quad (26)$$

where λ_q 's are the symplectic eigenvalues of the covariance matrices of the Gaussian quantum states and the function $h_o(\cdot)$ outputs the Holevo information for $q = 1$ and 2 :

$$h_o(\lambda_q) \triangleq \left(\frac{\lambda_q + 1}{2}\right) \log_2 \left(\frac{\lambda_q + 1}{2}\right) - \left(\frac{\lambda_q - 1}{2}\right) \log_2 \left(\frac{\lambda_q - 1}{2}\right). \quad (27)$$

It is noted that q takes two values which correspond to the eigenvalues of the two covariance matrices corresponding to the quantum states. The first covariance matrix is the covariance matrix of Eve's state, which, for each i -th channel is expressed as follows:

$$\Sigma_{E_i} = \begin{bmatrix} V_{e o_i} \mathbf{I}_2 & V_{c_i} \mathbf{Z} \\ V_{c_i}^* \mathbf{Z}^T & V_e \mathbf{I}_2 \end{bmatrix}, \quad (28)$$

where $V_{e o_i} \triangleq (1 - \beta_i) V_a + \beta_i V_e + \sigma_{\text{RIS}_i}^2$ and $V_{c_i} \triangleq \sqrt{\beta_i (V_e^2 - 1)}$. Recall that V_e is the variance of Eve's generated quantum state. Furthermore, \mathbf{Z} is the Pauli-z matrix expressed as $\text{diag}(1, -1)$. Thus, the symplectic eigenvalues of Σ_{E_i} are computed using the results in [48], [59] as:

$$\lambda_{i,1,2} = \sqrt{\frac{1}{2} \left(\nabla_i \pm \sqrt{\nabla_i^2 - 4 \det(\Sigma_{E_i})} \right)}, \quad (29)$$

where we have used the definitions:

$$\nabla_i \triangleq (1 - \beta_i)^2 (V_a^2 + V_e^2) + 2\beta_i (1 - \beta_i) V_a V_e + 2\beta_i + 2((1 - \beta_i) V_a + \beta_i V_e) \sigma_{\text{RIS}_i}^2 + \sigma_{\text{RIS}_i}^4, \quad (30)$$

$$\det(\Sigma_{E_i}) \triangleq ((1 - \beta_i) V_a V_e + \sigma_{\text{RIS}_i}^2 V_e + \beta_i)^2. \quad (31)$$

Thus, the Von Neumann entropy of Eve's state is obtained as:

$$S(E_i) = h_o(\lambda_{i1}) + h_o(\lambda_{i2}). \quad (32)$$

The second covariance matrix $\Sigma_{E_i | Q_{b_i}}$ corresponds to Eve's conditional state given Bob's measurement. Thus, when Bob performs a homodyne or heterodyne measurement, this matrix can be determined using general Gaussian measurements, and it is thus given for each i -th channel as follows:

$$\Sigma_{E_i | Q_{b_i}} = \Sigma_{E_i} - \frac{1}{V_{b_i}} \mathbf{W}_i \mathbf{\Pi} \mathbf{W}_i^\dagger, \quad (33)$$

where we have used the matrix definitions:

$$\mathbf{\Pi} \triangleq \begin{cases} \text{diag}(1, 0), & \text{homodyne} \\ \text{diag}(1, 1), & \text{heterodyne} \end{cases}, \quad (34a)$$

$$\mathbf{W}_i \triangleq \begin{bmatrix} \xi_i \mathbf{I}_2 \\ \varsigma_i \mathbf{Z} \end{bmatrix}, \quad (34b)$$

as well as the parameter:

$$V_{b_i} = \begin{cases} \beta_i V_o + (1 - \beta_i) V_e + \nu_{en} + \sigma_{\text{RIS}_i}^2, & \text{homodyne} \\ \beta_i V_o + (1 - \beta_i) V_e + 2\nu_{en} + 1 + \sigma_{\text{RIS}_i}^2, & \text{heterodyne} \end{cases}, \quad (34c)$$

Substituting (34a), (34b), and (34c) in (33) followed by algebraic simplifications results in the following expression:

$$\Sigma_{E_i | Q_{b_i}} = \begin{bmatrix} \mathbf{A}_i & \mathbf{C}_i \\ \mathbf{C}_i^\dagger & \mathbf{B}_i \end{bmatrix}, \quad (35)$$

which is of the same form as (28), and thus, its symplectic eigenvalues can be computed as follows:

$$\lambda_{i3,4} = \sqrt{\frac{1}{2} \left(\tilde{\nabla}_i \pm \sqrt{\tilde{\nabla}_i^2 - 4\det(\Sigma_{E_i|Q_{b_i}})} \right)}, \quad (36)$$

where we used the definitions:

$$\tilde{\nabla}_i \triangleq \det(\mathbf{A}_i) + \det(\mathbf{B}_i) + 2\det(\mathbf{C}_i), \quad (37)$$

$$\mathbf{A}_i \triangleq \text{diag} \left(\left(V_{eoi} - \frac{\xi_i^2}{V_{bi}}, V_{eoi} \right), \right), \quad (38)$$

$$\mathbf{B}_i \triangleq \text{diag} \left(\left(V_e - \frac{\zeta_i^2}{V_{bi}}, V_e \right), \right), \quad (39)$$

$$\mathbf{C}_i \triangleq \text{diag} \left(\left(V_{ci} - \frac{\xi_i \zeta_i}{V_{bi}}, -V_{ci} \right), \right), \quad (40)$$

$$\xi_i \triangleq \sqrt{\beta_i(1-\beta_i)}(V_e - V_a) + \sigma_{\text{RIS}_i}^2, \quad (41)$$

$$\zeta_i \triangleq \sqrt{(1-\beta_i)(V_e^2 - 1)}. \quad (42)$$

Hence, the conditional Von Neumann entropy of Eve's state given Bob's measurement is given by:

$$S(E_i|Q_{b_i}) = h_o(\lambda_{i3}) + h_o(\lambda_{i4}) \quad (43)$$

with $h_o(\cdot)$ given in (27), and λ_{i3} and λ_{i4} given in (36).

B. Closed-Form SKR Formula

By using (23), (24), and (25), the SKR of the considered RIS-assisted MIMO CV-QKD system employing collective entanglement attack and RR at Bob's side is obtained as:

$$\begin{aligned} \text{SKR}_{\text{MIMO}}^{\text{RR}} &= \left(1 - \frac{L_p}{T_c} \right) \\ &\times \sum_{i=1}^r \left(\frac{\eta d_m}{2} \log_2 \left(1 + \frac{\beta_i V_s}{\beta_i V_o + (1-\beta_i)V_e + \sigma_d^2 + \sigma_{\text{RIS}_i}^2} \right) \right. \\ &\quad \left. - h_o(\lambda_{i1}) - h_o(\lambda_{i2}) + h_o(\lambda_{i3}) + h_o(\lambda_{i4}) \right). \quad (44) \end{aligned}$$

VI. NUMERICAL RESULTS AND DISCUSSION

This section presents numerical results validating the analytical framework outlined in the previous sections. The simulation studies were carried out considering standard system parameters. The THz frequency was set as $f_c = 15$ THz considering $T_e = 297$ K, and the atmospheric absorption coefficient was chosen as $\rho = 50$ dB/km. The antenna gain was set as $G_a = 30$ dBi, the pilot power was $V_p = 60$ dB, and the variance of Alice's modulated signal was chosen as $V_a = V_s + V_o$ with $V_s = 1$ and V_o as discussed in Section III (i.e., $V_o = 2\bar{n} + 1$ with $\bar{n} = [\exp(hf_c/k_B T_e) - 1]^{-1}$). We have assumed that all K unit cells of the RIS share the same phase configuration, i.e., $\phi_k = \phi \forall k \in \{1, \dots, K\}$.

Fig. 2 illustrates the SKR (in bits/channel use) versus the transmission distance d (in meters) between Alice and Bob for various MIMO configurations considering $K = 100$ RIS unit elements and reconciliation efficiency $\eta = 0.95$. The plots were obtained using (44) and the values of d_m , $\sigma_{d_i}^2$, and $\lambda_{i_t} \forall t \in \{1, \dots, 4\}$ depended on the choice for homodyne and heterodyne measurements, as given in (34b) and (35).

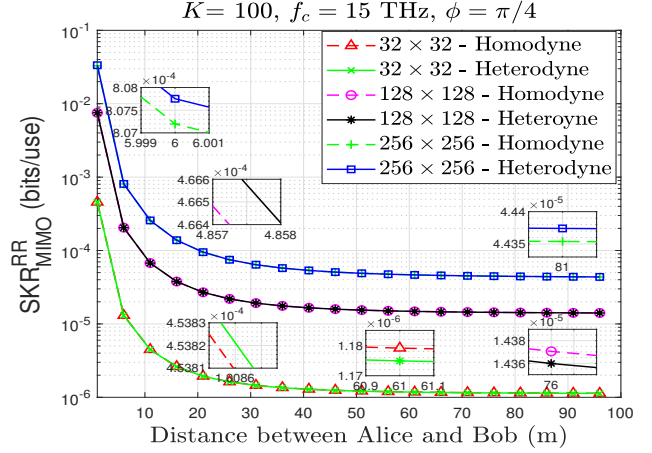


Fig. 2: SKR versus the transmission distance between Alice and Bob for $N_T = N_R = \{32, 128, 256\}$, $f_c = 15$ THz, $K = 100$, and $\phi = \pi/4$, with Bob employing homodyne and heterodyne measurements for secret key detection.

The ML estimate $\hat{\mathbf{C}}_{\text{RML}}$ obtained in (22) was used in (23) for the evaluation of the noise variance arising due to the channel estimation error $\sigma_{\text{RIS}_i}^2$. It can be observed from the figure that, in the 256×256 MIMO configuration, the SKR obtained by employing heterodyne detection is higher than that obtained when Bob employs homodyne measurements. This trend is consistent for all distance values between Alice and Bob. However, for lower MIMO configurations, such as the considered 128×128 and 32×32 case, it is observed that heterodyne measurements result in a higher SKR value at lower distance values; this trend becomes reversed at higher distances. This behavior can be justified from the fact that, for lower MIMO configurations, the noise caused by heterodyne detection (due to the exposure of both the position and momentum quadrature) is greater than that of homodyne detection at higher distances between the transceiver pair. In addition, the SKR of the system increases when N_T and N_R are increased. It can also be seen that SKR saturates at higher distance values, which can be attributed to the use of the RIS, without which the SKR would reduce with increasing distance between Alice and Bob.

The SKR as a function of the pilot power V_p for different RIS-assisted MIMO configurations at a constant transmission distance of $d = 100$ m, with Bob conducting either homodyne or heterodyne measurements, is depicted in Fig. 3. As shown, the performance of heterodyne detection surpasses that of homodyne detection at lower V_p values, and the gap between the SKRs arising due to these two measurements is more prominent at higher values of N_T and N_R . It can be also observed that the SKR degrades with increasing V_p . This can be intuitively understood from the fact that a higher pilot power implies a longer duration for channel estimation, resulting in a lower duration for secret key transmissions, thus, leading to SKR values. This effect is also mathematically evident from expression (21) where the duration of the pilot symbol occurs both in the summation term and in the denominator, thus, nullifying the effect of the increased pilot power in the

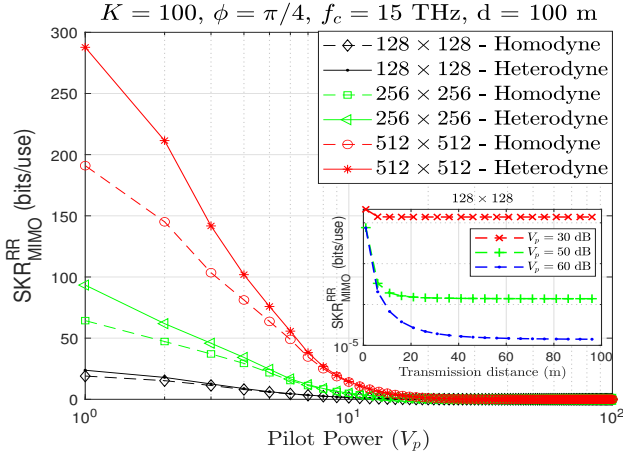


Fig. 3: SKR versus the pilot power V_p for $N_T = N_R = \{128, 256, 512\}$ MIMO configurations, $f_c = 15$ THz, $d = 100$ m, $K = 100$, and $\phi = \pi/4$, with Bob employing homodyne and heterodyne measurements for secret key detection.

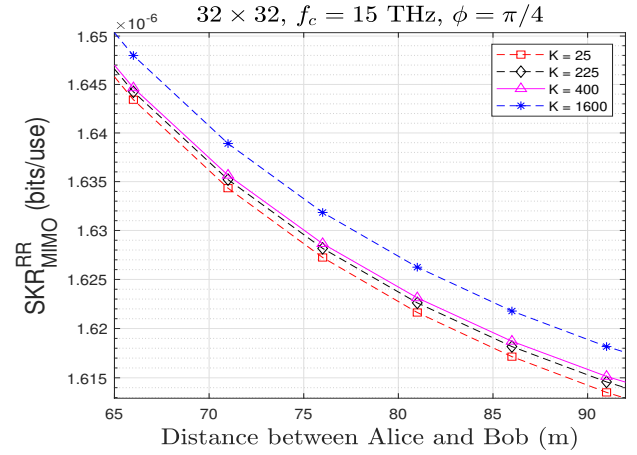


Fig. 5: SKR versus transmission distance d between Alice and Bob for a 32×32 MIMO configuration, $f_c = 15$ THz, $\phi = \pi/4$ for $K = \{25, 225, 400, 1600\}$ RIS elements, with homodyne detection at Bob's side.

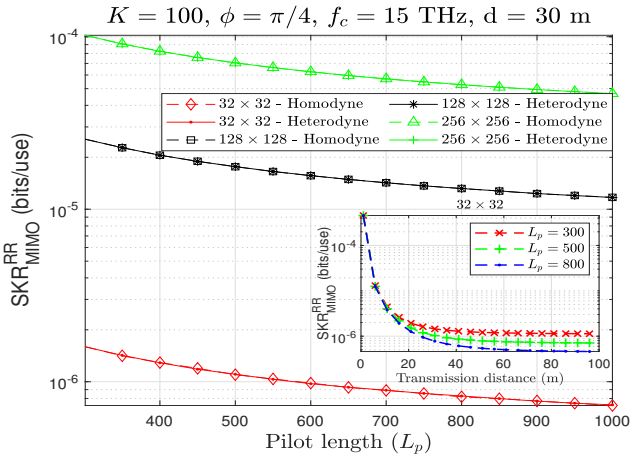


Fig. 4: SKR versus the pilot length L_p for $N_T = N_R = \{32, 128, 256\}$ MIMO configurations, $f_c = 15$ THz, $d = 30$ m, $K = 100$, $\phi = \pi/4$, with Bob employing homodyne and heterodyne measurements for secret key detection.

estimation of the noise variance. As seen in the figure, this effect is valid for all d values. There is also a saturation effect becoming prominent at lower transmission distances for lower pilot power values.

The impact of pilot duration on the SKR performance of the considered RIS-assisted MIMO CV-QKD system is showcased in Fig. 4, which demonstrates the SKR for both homodyne and heterodyne measurements conducted by Bob for varying values of N_T and N_R at a constant transmission distance of $d = 30$ m between Alice and Bob. Similar to Fig. 3, SKR degrades as L_p increases. This is indicative of the fact that the impact of pilot length is greater on the noise covariance, as demonstrated in (21). Therein, the summation over the L_p term predominates the $1/L_p$ component (see (21) and (22)). However, contrary to the observation in Fig. 3, the values of the SKR do not merge irrespective of the chosen MIMO configuration. Furthermore, there is a negligible difference in

the performance of the homodyne and heterodyne detectors for varying L_p . Additionally, the saturation effect is not as prominent with increasing L_p as it was with increasing V_p . A similar trend to V_p is also observed for different values of L_p at d values. However, in contrast to Fig. 3, the effect of L_p on the SKR is more prominent at higher values of d .

The advantage of employing an RIS to achieve a higher SKR is illustrated in Fig. 5, which depicts SKR with respect to different d and K values for a 32×32 MIMO configuration and $\phi = \pi/4$. It is demonstrated that the SKR of the system improves with increasing K , and this improvement becomes slightly larger for larger d values. However, it is observed that the difference between the curves is small as compared to the order in which the number of elements in the RIS is increased. Thus, a small RIS becomes practical to be deployable for such systems.

Finally, the effect of the variation of the common phase shift ϕ of all RIS elements on the system's SKR performance is demonstrated in Fig. 6. It is noted that, to the best of our knowledge, this is the first work proposing the use of RISs for such quantum communication systems employing a practical channel estimation scheme, thus, it is our goal to show the SKR behaviour for various ϕ values. As shown, SKR depends on ϕ in a sinusoidal manner. This implies that there exists an optimal ϕ maximizing the SKR performance. Table I includes such values for some of the system parameters. It can be seen that both V_p and d values play a crucial role in the optimal ϕ maximizing SKR. For a given MIMO configuration, increasing the value of V_p at a given distance, initially reduces the value of the optimal ϕ , which then tends to saturate at higher values of V_p . However, there is no such straightforward trend for the relation of the optimal ϕ with value of d , which can be attributed to the highly non-linear nature of the THz channel model. Similarly holds for the relation between the optimal ϕ and the $N_T = N_R$ values.

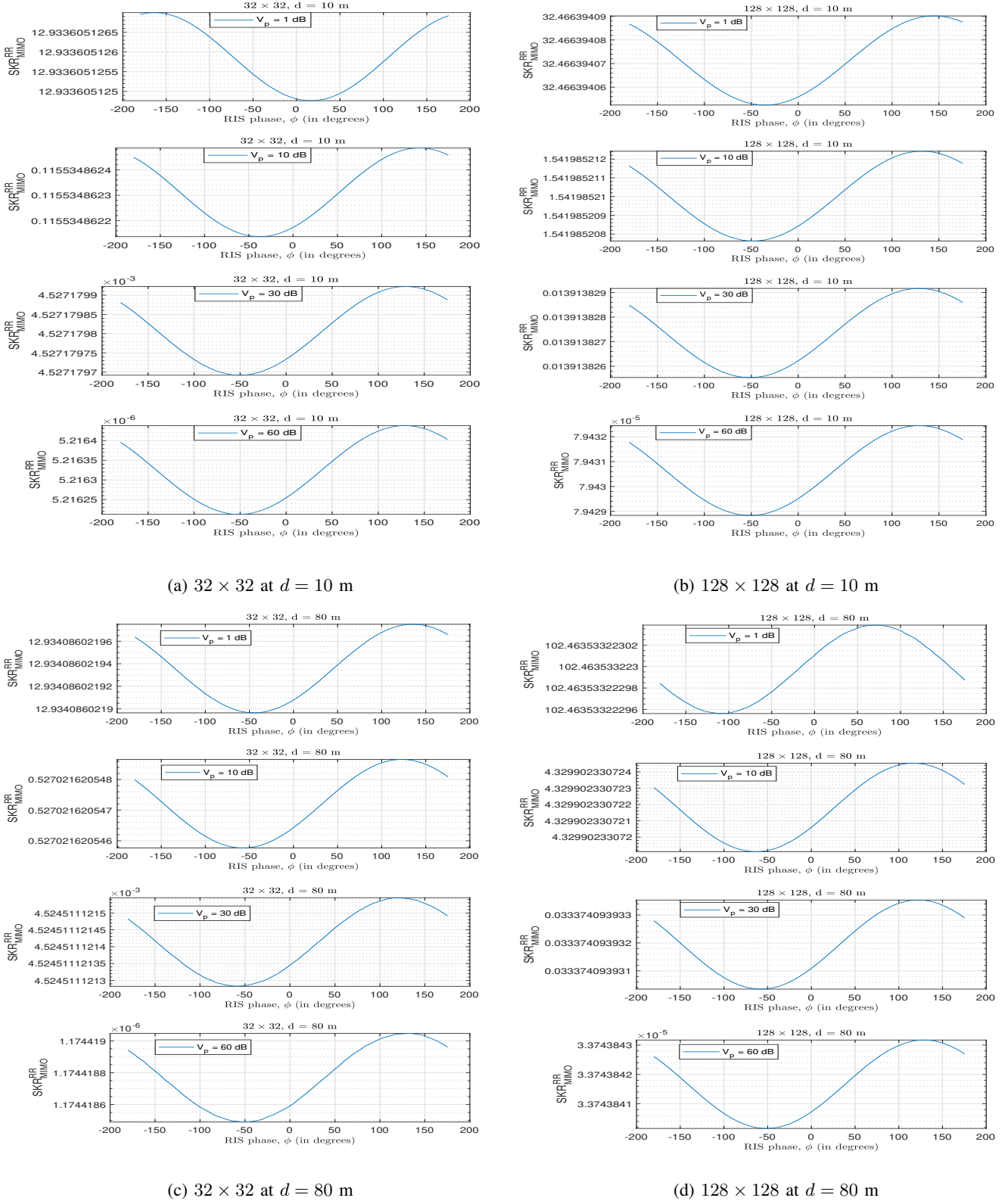


Fig. 6: SKR versus the RIS phase configuration ϕ for $N_T = N_R = \{32, 12\}$ MIMO configurations, $f_c = 15$ THz, $d = \{10, 80\}$ m, and $K = 100$, with Bob employing heterodyne detection for secret key detection.

VII. CONCLUSIONS

This paper presented an RIS-assisted point-to-point MIMO communication system operating at THz frequencies where the

transmitter, Alice, employs CV-QKD to transmit secret keys to the receiver, Bob. We considered the practical case where Bob performs LS-based channel estimation and feeds back

TABLE I: Optimal phase value for all RIS elements for $N_T = N_R = \{16, 32, 64, 128\}$, pilot powers $V_p = \{1, 10, 30, 60\}$ dB, and distances between Alice and Bob $d = \{10, 50, 80\}$ m.

$N_T = N_R$	Optimal phase shift, ϕ , of RIS elements											
	$d = 10$ m				$d = 50$ m				$d = 80$ m			
	$V_p = 1$ dB	$V_p = 10$ dB	$V_p = 30$ dB	$V_p = 60$ dB	$V_p = 1$ dB	$V_p = 10$ dB	$V_p = 30$ dB	$V_p = 60$ dB	$V_p = 1$ dB	$V_p = 10$ dB	$V_p = 30$ dB	$V_p = 60$ dB
16	-128.43°	72.10°	158.05°	129.40°	-151.35°	-99.78°	112.20°	129.40°	43.45°	100.75°	-2.38°	129.40°
32	-162.81°	140.86°	129.40°	129.40°	152.32°	77.83°	129.40°	129.40°	135.13°	123.67°	117.94°	129.40°
64	-180°	-105.52°	-134.16°	129.40°	-139.89°	72.10°	135.13°	129.40°	-162.81°	-162.81°	112.21°	129.40°
128	146.59°	129.40°	129.40°	129.40°	-180°	-162.81°	129.40°	129.40°	102.46°	117.94°	123.66°	129.40°

the MIMO channel coefficients to Alice, prior to receiving secret keys from her. An eavesdropper, Eve, was considered to intercept the secret key transmission, eavesdropping first the feedback channel with the channel estimation information, and then, during the secret key transmission, applying a collective Gaussian attack. Considering that Bob utilizes either homodyne or heterodyne detection for the reception of the secret key, we presented a novel expression for the SKR performance of the system. Extensive numerical results were presented to corroborate the analytical framework of the paper and indicate the variation of the system performance over different parameters. It was showcased that an RIS plays a crucial role in improving SKR, preventing this metric's degradation at higher link distances, and that there exists an optimal RIS phase configuration that boosts SKR even further. This optimal configuration was shown numerically to depend on the pilot signal power and the link distance. It was also demonstrated that heterodyne detection is preferable over homodyne at lower pilot symbol powers, providing additional design benefits for the RIS-assisted MIMO CV-QKD communication systems at the THz frequency band.

REFERENCES

- [1] S. P. Dash, S. Joshi, S. C. Satapathy, S. K. Shandilya, and G. Panda, "A cybertwin-based 6G cooperative IoE communication network: Secrecy outage analysis," *IEEE Trans. Indus. Inform.*, vol. 18, no. 7, pp. 4922–4932, Jul. 2022.
- [2] M. Giordani, M. Polese, M. Mezzavilla, S. Rangan, and M. Zorzi, "Toward 6G networks: Use cases and technologies," *IEEE Commun. Mag.*, vol. 58, no. 3, pp. 55–61, Mar. 2020.
- [3] R. Nissel, "Correctly modeling TX and RX chain in (distributed) massive MIMO—New fundamental insights on coherency," *IEEE Commun. Lett.*, vol. 26, no. 10, pp. 2465–2469, Oct. 2022.
- [4] M. Guo and M. C. Gursoy, "Joint activity detection and channel estimation in cell-free massive MIMO networks with massive connectivity," *IEEE Trans. Commun.*, vol. 70, no. 1, pp. 317–331, Jan. 2022.
- [5] J. Xu, L. You, G. C. Alexandropoulos, X. Yi, W. Wang, and X. Gao, "Near-field wideband extremely large-scale MIMO transmissions with holographic metasurface-based antenna arrays," *IEEE Trans. Wireless Commun.*, vol. 23, no. 9, pp. 12 054–12 067, Sep. 2024.
- [6] C. Huang, A. Zappone, G. C. Alexandropoulos, M. Debbah, and C. Yuen, "Reconfigurable intelligent surfaces for energy efficiency in wireless communication," *IEEE Trans. Wireless Commun.*, vol. 18, no. 8, pp. 4157–4170, Aug. 2019.
- [7] M. Di Renzo, M. Debbah, D.-T. Phan-Huy, A. Zappone, M.-S. Alouini, C. Yuen, V. Sciancalepore, G. C. Alexandropoulos, J. Hoydis, H. Gacanin, J. de Rosny, A. Bounceur, G. Lerosey, and M. Fink, "Smart radio environments empowered by reconfigurable AI meta-surfaces: An idea whose time has come," *EURASIP J. Wireless Commun. Netw.*, vol. 2019, no. 1, p. 129, May 2019.
- [8] R. K. Pal, S. P. Dash, S. Aïssa, and D. Ghose, "Outage probability analysis of RIS-assisted indoor wide-FOV-VLC/RF wireless communication," *IEEE Wireless Commun. Lett.*, vol. 13, no. 1, pp. 34–38, Jan. 2024.
- [9] M. A. Jamshed, A. Kaushik, M. Toka, W. Shin, M. Z. Shaker, S. P. Dash, and D. Dardari, "Synergizing airborne non-terrestrial networks and reconfigurable intelligent surfaces-aided 6G IoT," *IEEE Internet of Things Mag.*, vol. 7, no. 2, pp. 46–52, Mar. 2024.
- [10] A. Basu, S. P. Dash, S. Joshi, and D. Ghose, "Performance of SSK-based receive diversity RIS-assisted system with Nakagami-m fading channels," in *2023 IEEE 97th Veh. Technol. Conf. (VTC2023-Spring)*, Florence, Italy, Aug. 2023, pp. 1–5.
- [11] I. F. Akyildiz, C. Han, Z. Hu, S. Nie, and J. M. Jornet, "Terahertz band communication: An old problem revisited and research directions for the next decade," *IEEE Trans. Commun.*, vol. 70, no. 6, pp. 4250–4285, Jun. 2022.
- [12] M. Shehata, K. Wang, J. Webber, M. Fujita, T. Nagatsuma, and W. Withayachumnankul, "IEEE 802.15.3d-compliant waveforms for terahertz wireless communications," *J. Lightwave Technol.*, vol. 39, no. 24, pp. 7748–7760, Dec. 2021.
- [13] C. Weedbrook, S. Pirandola, R. García-Patrón, N. J. Cerf, T. C. Ralph, J. H. Shapiro, and S. Lloyd, "Gaussian quantum information," *Rev. Mod. Phys.*, vol. 84, no. 2, p. 621, May 2012.
- [14] A. Manzalini, "Quantum communications in future networks and services," *Quantum Rep.*, vol. 2, no. 1, pp. 221–232, Mar. 2020.
- [15] W. Diffie and M. Hellman, "New directions in cryptography," *IEEE Trans. Inf. Theory*, vol. 22, no. 6, pp. 644–654, Nov. 1976.
- [16] N. K. Kundu, S. P. Dash, M. R. McKay, and R. K. Mallik, "Channel estimation and secret key rate analysis of MIMO terahertz quantum key distribution," *IEEE Trans. Commun.*, vol. 70, no. 5, pp. 3350–3363, May 2022.
- [17] I. B. Djordjevic, "Hybrid QKD protocol outperforming both DV- and CV-QKD protocols," *IEEE Photon. J.*, vol. 12, no. 1, pp. 1–8, Feb. 2020.
- [18] C. Ware, R. Aymeric, C. Zidi, and M. Lourdiane, "Potential impact of CV-QKD integration on classical WDM network capacity," *IEEE Photon. Technol. Lett.*, vol. 34, no. 18, pp. 957–960, Sep. 2022.
- [19] R. Lin and J. Chen, "Modeling and minimizing spontaneous Raman scattering for QKD secured DWDM networks," *IEEE Commun. Lett.*, vol. 25, no. 12, pp. 3918–3921, Dec. 2021.
- [20] V. Scarani, H. Bechmann-Pasquucci, N. J. Cerf, M. Dušek, N. Lütkenhaus, and M. Peev, "The security of practical quantum key distribution," *Rev. Mod. Phys.*, vol. 81, pp. 1301–1350, Sep. 2009.
- [21] I. B. Djordjevic, "Optimized-eight-state CV-QKD protocol outperforming Gaussian modulation based protocols," *IEEE Photonics Journal*, vol. 11, no. 4, pp. 1–10, Jun. 2019.
- [22] E. Hugues-Salas, O. Alia, R. Wang, K. Rajkumar, G. T. Kanellos, R. Nejabati, and D. Simeonidou, "11.2 Tb/s classical channel coexistence with DV-QKD over a 7-core multicore fiber," *J. Lightwave Technol.*, vol. 38, no. 18, pp. 5064–5070, Sep. 2020.
- [23] O. Alia, R. S. Tessinari, E. Hugues-Salas, G. T. Kanellos, R. Nejabati, and D. Simeonidou, "Dynamic DV-QKD networking in trusted-node-free software-defined optical networks," *J. Lightwave Technol.*, vol. 40, no. 17, pp. 5816–5824, Sep. 2022.
- [24] J. Lodewyck, M. Bloch, R. García-Patrón, S. Fossier, E. Karpov, E. Diamanti, T. Debuisschert, N. J. Cerf, R. Tualle-Brouri, S. W. McLaughlin *et al.*, "Quantum key distribution over 25 km with an all-fiber continuous-variable system," *Phys. Rev. A*, vol. 76, no. 4, p. 042305, Oct. 2007.
- [25] Z. Yichen, B. Yiming, L. Zhengyu, Y. Song, and G. Hong, "Continuous-variable quantum key distribution system: Past, present, and future," *Appl. Phys. Rev.*, vol. 11, no. 011318, Mar. 2024.
- [26] M. Jian, G. C. Alexandropoulos, E. Basar, C. Huang, R. Liu, Y. Liu, and C. Yuen, "Reconfigurable intelligent surfaces for wireless communica-

- tions: Overview of hardware designs, channel models, and estimation techniques," *Intell. Conver. Netw.*, vol. 3, no. 1, pp. 1–32, Mar. 2022.
- [27] A. P. Ajayan, S. P. Dash, and B. Ramkumar, "Approximate composite channel statistics and performance analysis of IRS-aided wireless system under Nakagami- m fading," *IEEE Access*, vol. 11, pp. 102 290–102 300, Sep. 2023.
- [28] G. C. Alexandropoulos, N. Shlezinger, and P. del Hougne, "Reconfigurable intelligent surfaces for rich scattering wireless communications: Recent experiments, challenges, and opportunities," *IEEE Commun. Mag.*, vol. 59, no. 6, pp. 28–34, Jun. 2021.
- [29] E. Basar, G. C. Alexandropoulos, Y. Liu, Q. Wu, S. Jin, C. Yuen, O. A. Dobre, and R. Schober, "Reconfigurable intelligent surfaces for 6G: Emerging hardware architectures, applications, and open challenges," *IEEE Veh. Technol. Mag.*, vol. 19, no. 3, pp. 27–47, Sep. 2024.
- [30] S. P. Dash and A. Kaushik, "RIS-assisted 6G wireless communications: A novel statistical framework in the presence of direct channel," *IEEE Commun. Lett.*, vol. 28, no. 3, pp. 717–721, Mar. 2024.
- [31] M. Najafi, B. Schmauss, and R. Schober, "Intelligent reflecting surfaces for free space optical communication systems," *IEEE Trans. Commun.*, vol. 69, no. 9, pp. 6134–6151, Sep. 2021.
- [32] E. C. Strinati, G. C. Alexandropoulos, H. Wymeersch, B. Denis, V. Sciancalepore, R. D'Errico, A. Clemente, D.-T. Phan-Huy, E. De Carvalho, and P. Popovski, "Reconfigurable, intelligent, and sustainable wireless environments for 6G smart connectivity," *IEEE Commun. Mag.*, vol. 59, no. 10, pp. 99–105, Oct. 2021.
- [33] Z. Chen, B. Ning, C. Han, Z. Tian, and S. Li, "Intelligent reflecting surface assisted terahertz communications toward 6G," *IEEE Wireless Commun.*, vol. 28, no. 6, pp. 110–117, Dec. 2021.
- [34] M. H. Kumar, S. Sharma, K. Deka, and V. Bhatia, "Intelligent reflecting surface assisted terahertz communications," in *2022 IEEE Int. Conf. Signal Process. Commun. (SPCOM)*, India, 2022, pp. 1–5.
- [35] S. Matos, Y. Ma, Q. Luo, J. Deuermeier, L. Lucci, P. Gavrilidis, A. Kiazadeh, V. Lain-Rubio, T. D. Phan, P. J. Soh, A. Clemente, L. M. Pessoa, and G. C. Alexandropoulos, "Reconfigurable intelligent surfaces for THz: Hardware impairments and switching technologies," in *Proc. Int. Conf. Electromagn. Adv. Appl.*, Lisbon, Portugal, 2024, pp. 551–555.
- [36] G. C. Alexandropoulos, D.-T. Phan-Huy, K. D. Katsanos, M. Crozzoli, H. Wymeersch, P. Popovski, P. Ratajczak, Y. Bénédic, M.-H. Hamon, S. H. Gonzalez, P. Mursia, M. Rossanese, V. Sciancalepore, J.-B. Gros, S. Terranova, G. Gradoni, P. Di Lorenzo, M. Rahal, B. Denis, R. D'Errico, A. Clemente, and E. C. Strinati, "RIS-enabled smart wireless environments: deployment scenarios, network architecture, bandwidth and area of influence," *EURASIP Journal on Wireless Communications and Networking*, vol. 2023, no. 1, p. 103, Oct. 2023.
- [37] G. C. Alexandropoulos, B. K. Jung, P. Gavrilidis, S. Matos, L. H. W. Loeser, V. Elesina, A. Clemente, R. D'Errico, L. M. Pessoa, and T. Kürner, "Characterization of indoor RIS-assisted channels at 304 GHz: Experimental measurements, challenges, and future directions," *arXiv preprint:2412.07359*, 2024.
- [38] G. C. Alexandropoulos, N. Shlezinger, I. Alamzadeh, M. F. Imani, H. Zhang, and Y. C. Eldar, "Hybrid reconfigurable intelligent metasurfaces: Enabling simultaneous tunable reflections and sensing for 6G wireless communications," *IEEE Veh. Technol. Mag.*, vol. 19, no. 1, pp. 75–84, Mar. 2024.
- [39] S. P. Dash, R. K. Mallik, and N. Pandey, "Performance analysis of an index modulation-based receive diversity RIS-assisted wireless communication system," *IEEE Commun. Lett.*, vol. 26, no. 4, pp. 768–772, Apr. 2022.
- [40] S. P. Dash, S. Joshi, and S. Aïssa, "Envelope distribution of two correlated complex Gaussian random variables and application to the performance evaluation of RIS-assisted communications," *IEEE Commun. Lett.*, vol. 26, no. 9, pp. 2018–2022, Sep. 2022.
- [41] A. Basu, S. P. Dash, A. Kaushik, D. Ghose, M. D. Renzo, and Y. C. Eldar, "Performance analysis of RIS-aided index modulation with greedy detection over Rician fading channels," *IEEE Trans. Wireless Commun.*, vol. 23, no. 8, pp. 8465–8479, Aug. 2024.
- [42] A. Basu, S. P. Dash, and D. Ghose, "RIS empowered index modulation-based receive diversity wireless system with Nakagami- m fading channels," *IEEE Trans. Veh. Technol.*, vol. 73, no. 6, pp. 8153–8168, Jun. 2024.
- [43] Y. Liu, C. Huang, G. Chen, R. Song, S. Song, and P. Xiao, "Deep learning empowered trajectory and passive beamforming design in UAV-RIS enabled secure cognitive non-terrestrial networks," *IEEE Wireless Commun. Lett.*, vol. 13, no. 1, pp. 188–192, Jan. 2024.
- [44] V. Jamali, H. Ajam, M. Najafi, B. Schmauss, R. Schober, and H. V. Poor, "Intelligent reflecting surface assisted free-space optical communications," *IEEE Commun. Mag.*, vol. 59, no. 10, pp. 57–63, Oct. 2021.
- [45] Z. Wang, R. Malaney, and J. Green, "Inter-satellite quantum key distribution at terahertz frequencies," in *2019 IEEE Int. Conf. Commun. (ICC)*, Shanghai, China, 2019, pp. 1–7.
- [46] C. Ottaviani, M. J. Woolley, M. Erementchouk, J. F. Federici, P. Mazumder, S. Pirandola, and C. Weedbrook, "Terahertz quantum cryptography," *IEEE J. Sel. Areas Commun.*, vol. 38, no. 3, pp. 483–495, Mar. 2020.
- [47] C. Liu, C. Zhu, X. Liu, M. Nie, H. Yang, and C. Pei, "Multicarrier multiplexing continuous-variable quantum key distribution at terahertz bands under indoor environment and in inter-satellite links communication," *IEEE Photon. J.*, vol. 13, no. 4, pp. 1–13, Aug. 2021.
- [48] N. K. Kundu, S. P. Dash, M. R. McKay, and R. K. Mallik, "MIMO terahertz quantum key distribution," *IEEE Commun. Lett.*, vol. 25, no. 10, pp. 3345–3349, Oct. 2021.
- [49] N. K. Kundu, M. R. McKay, R. Murch, and R. K. Mallik, "Intelligent reflecting surface-assisted free space optical quantum communications," *IEEE Trans. Wireless Commun.*, vol. 23, no. 5, pp. 5079–5093, May 2024.
- [50] S. Kumar and S. P. Dash, "RIS-assisted THz MIMO wireless system in the presence of direct link for CV-QKD with limited quantum memory," 2024. [Online]. Available: <https://arxiv.org/abs/2410.16731>
- [51] S. W. Ellingson, "Path loss in reconfigurable intelligent surface-enabled channels," in *Proc. IEEE Int. Symp. Personal, Indoor Mobile Radio Commun. (PIMRC)*. Helsinki, Finland, Sep. 2021, pp. 829–835.
- [52] M. He, J. Xu, W. Xu, H. Shen, N. Wang, and C. Zhao, "RIS-assisted quasi-static broad coverage for wideband mmWave massive MIMO systems," *IEEE Trans. Wireless Commun.*, vol. 22, no. 4, pp. 2551–2565, Apr. 2023.
- [53] I.-P. Hong, "Reviews based on the reconfigurable intelligent surface technical issues," *Electronics*, vol. 12, no. 21, pp. 1–48, Nov. 2023.
- [54] N. Hosseini-dehaj, Z. Babar, R. Malaney, S. X. Ng, and L. Hanzo, "Satellite-based continuous-variable quantum communications: State-of-the-art and a predictive outlook," *IEEE Commun. Surveys Tut.*, vol. 21, no. 1, pp. 881–919, Aug. 2019.
- [55] V. Jamali, G. C. Alexandropoulos, R. Schober, and H. V. Poor, "Low-to-zero-overhead IRS reconfiguration: Decoupling illumination and channel estimation," *IEEE Commun. Lett.*, vol. 26, no. 4, pp. 932–936, Apr. 2022.
- [56] C. Gianfranco, *Quantum Communications*. University of Padova, Padova, Italy: Springer, 2015, ch. Fundamentals of Continuous Variables, pp. 475–484.
- [57] N. K. Kundu, M. R. McKay, A. Conti, R. K. Mallik, and M. Z. Win, "MIMO terahertz quantum key distribution under restricted eavesdropping," *IEEE Trans. Quantum Engineering*, vol. 4, pp. 1–15, Apr. 2023.
- [58] M. McKay and I. Collings, "General capacity bounds for spatially correlated Rician MIMO channels," *IEEE Trans. Inf. Theory*, vol. 51, no. 9, pp. 3121–3145, Sep. 2005.
- [59] C. Weedbrook, S. Pirandola, S. Lloyd, and T. C. Ralph, "Quantum cryptography approaching the classical limit," *Phys. Rev. Lett.*, vol. 105, p. 11, Sep. 2010.
- [60] C. Weedbrook, S. Pirandola, and T. C. Ralph, "Continuous-variable quantum key distribution using thermal states," *Phys. Rev. A*, vol. 86, no. 2, p. 022318, Aug. 2012.